Elastic topological interface states and voltage feeder by breaking inversion symmetry on thin plates

Dongwoo Lee,[1] N. D. Lanzillotti-Kimura,[2] Jensen Li,[3] and Junsuk Rho ●[1,4,5,*]

[1]*Department of Mechanical Engineering, Pohang University of Science and Technology (POSTECH), Pohang 37673, Republic of Korea*
[2]*Université Paris-Saclay, CNRS, Centre de Nanosciences et de Nanotechnologies (C2N), 91120 Palaiseau, France*
[3]*Department of Physics, The Hong Kong University of Science and Technology, Clear Water Bay, Kowloon, Hong Kong, China*
[4]*Department of Chemical Engineering, Pohang University of Science and Technology (POSTECH), Pohang 37673, Republic of Korea*
[5]*POSCO-POSTECH-RIST Convergence Research Center for Flat Optics and Metaphotonics, Pohang 37673, Republic of Korea*

The rapid progress in the engineering of topological edge/interface states has attracted considerable interest in both photonic and phononic systems originating from their electronic equivalent systems. However, most classical wave types, such as electromagnetic/acoustic waves in topological engineering, are described by two-dimensional (2D) partial differential equations (PDEs), which are not suitable for thin plate motions. We present a 1D elastic topological interface state induced by symmetry breaking to bridge a knowledge gap in 4D PDE, particularly for flexural waves on thin-plate frameworks. We also leverage the localized state at the interface for energy harvesting, which can provide a sufficiently high voltage feeder by piezoelectric effects.

I. INTRODUCTION

The condensed energy in highly confined waves can be harnessed for energy harvesting by converting elastic or acoustic waves being dissipated to electric resources [1–6]. To enable such localized energy, several studies have been actively pursued and some representative platforms such as gradient index [7–13], local resonant [14–18], defect-based [19–26] artificial materials have been developed. Such platforms are potentially promising candidates for next-generation elastic energy transport at the desired location with robust amplification. Gradient index phononic crystals [7–13] guide elastic waves with varying effective material properties in a space-parametric fashion, but do not achieve a significant level of localized energy. Local resonant structures, which consist of extra local resonators attached to the main structural body, have been actively developed [14–18]. These designs enable the suppression of elastic wave propagation while local resonators capture elastic energy. In general, the local resonance mechanism generates leaky modes, hence for the localization aspect, the efficiency in terms of quality factor is less than that of the elastic version of the bound state in the continuum models [27,28]. Defect-based phononic crystals also have evolved by introducing a defect to break periodicity in dispersion relation with a partial impurity, which gives rise to flat bands with extremely low slope (zero group velocity), indicating that elastic waves are densely distributed exclusively in the impurity domain [19–26]. To date, however, the efficiency of localization is indeed bound by the amplitude of the confined mode of elastic waves capable of producing millivolts.

Recently, the development of elastic topological phononic crystals [29–33] and metamaterials [34–38] originating from mathematics and condensed matter physics [39–41] has garnered considerable attention. Topological edge states that are gapless in bulk bands with topological protection are confined at the boundary and pass through the topological bandgap in momentum space, according to the bulk-edge correspondence [29]. These topologically protected features enable them to be immune to structural defects, resulting in resilient wave propagation along desired boundaries while limiting bulk propagation. Additionally, in a lower dimension (from the boundary mode to singular point mode), a highly localized so-called interface state can be sought, accompanied by reflection-free behavior [42–44]. Emphasis has been placed heavily on the exceptional carrier of elastic energy transfer as a cutting-edge waveguide employing topological mode inversion supported by helical and valley modes in elastic continuum models for two-dimentional (2D) systems [32,37,45,46]. For more details on the physical context of generic elastic topological systems and their various waveguide designs, please visit [47,48]. In one-dimensional (1D) systems, however, most of the relevant studies are based on discrete chain models, therefore there is a strong demand to explore continuous elastic systems [34,49,50]. Particularly for an interface state in a thin plate framework, the approach for constructing topological systems has not been well investigated owing to the higher-order governing equation than that of other classical waves, which makes it challenging to unveil. Moreover, such an interface state has promising potential use for efficient energy capture as a novel kind of voltage feeder through the piezoelectric effect, opening up exciting possibilities for the localization of gigantic vibration energy.

In this work, we propose topological interface states that leverage a mirror symmetry in elastic phononic crystals (PCs). In particular, the system for flexural waves described by four-dimensional (4D) partial differential equations (PDEs) is considered, as opposed to 2D PDEs that have been commonly
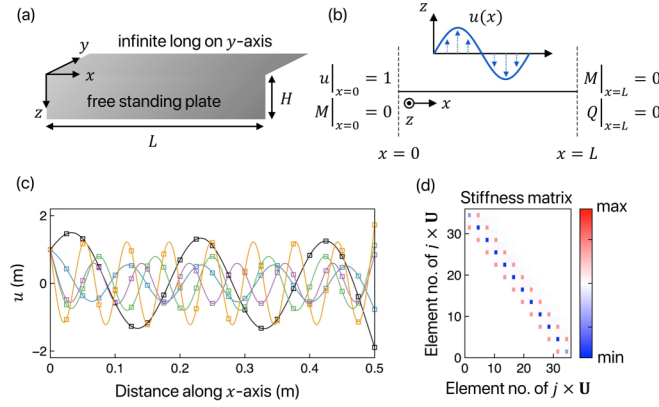
*jsrho@postech.ac.kr

FIG. 1. (a) Schematic of the bare steel plate with geometrical dimensions L and H. (b) Mathematical schematic of the 1D plate model with nonhomogeneous, simply supported, and free edge boundary conditions. (c) Analytic solutions (solid line) of out-of-plane displacement fields in comparison to numerical solutions (dotted square) using weak formulation at frequencies of 10 kHz (black), 30 kHz (blue), 50 kHz (green), 70 kHz (violet), and 90 kHz (orange). (d) Distribution of the stiffness matrix considering nodes and unknown variables given by discretized mesh and corresponding boundary conditions, with its elements being highly localized around the diagonal elements.

handled in topological engineering. We construct multilayered PCs that are topologically trivial estimated by the planewave expansion method, resulting in a bandgap feature. By breaking the inversion symmetry in such a system, a localized interface state arising from a geometric phase (so-called Zak phase) transition is obtained. Moreover, the feasibility of employing the localized state as a voltage feeder in energy harvesting is examined, with the resultant voltages in the few tens of volts range. Our findings reveal that establishing highly confined waves and high voltages requires an optimized system that takes evanescent wave couplings between the input and interface into account.

II. PROBLEM STATEMENT

Elastic waves in bulk media present a rich palette of wave polarizations such as longitudinal, transverse, and torsional modes. The geometrical shape of the thin plate system implies the motion of the guided wave. Plate motions in Lamb modes are characterized by symmetric and antisymmetric deformations along the plate thickness and boundary conditions. For these reasons, dealing with elastic waves rather than other classical waves (e.g., acoustic waves) entails more complexity. In this work, we look at the antisymmetric deformation of thin plates, also known as flexural waves, which propagate in the lateral dimension direction. For simplicity, we suppose that the plate medium is homogeneous and isotropic, with no in-plane (or transverse shear) deformation [Fig. 1(a)]. Thus, the harmonic plate motion can be described by using Kirchhoff-Love (K-L) plate theory, as written by

$$D\Delta^2 u = -2\rho h \ddot{u} - q, \tag{1}$$

where $\Delta^2 \equiv \nabla^2 \nabla^2$ is the biharmonic operator, u is the out-of-plane displacement field, and q is a negligible external load. ρ denotes the mass density, h is the half thickness of the plate, and D is the flexural rigidity [$= 2h^3 E/3(1 - \nu^2)$] where E and ν is the Young's modulus and the Poisson's ratio, respectively. Assuming that the solution u is time harmonic dependent and there is no strain on the y axis, the 1D partial differential equation (PDE) is formulated as $\partial^4 u/\partial x^4 = \gamma^4 u$ where $\gamma = (2\rho h \omega^2/D)^{1/4}$. Here, we examine a simplifying model for the 1D case with the following boundary conditions to be solved, assuming that [Fig. 1(b)]:

$$u|_{x=0} = 1, \tag{2a}$$

$$M|_{x=0} = 0, \tag{2b}$$

$$M|_{x=L} = 0, \tag{2c}$$

$$Q|_{x=L} = 0, \tag{2d}$$

where the bending moment M and the shearing force Q are related to u'' and $-u'''$. The nonhomogeneous simply supported condition [51] of Eqs. (2a) and (2b) is employed to have an eigendisplacement loading at $x = 0$ rather than employing the additional external load q and to avoid the duplicated loading conditions, while Eqs. (2c) and (2d) at $x = L$ indicate the free edge boundary. We obtain the following analytical form by solving with four boundary conditions:

$$u(x) = -\csc \gamma L (\sinh \gamma L + \cosh \gamma L)(\cosh \gamma L (\sin \gamma (L - x) + \cos \gamma L \sinh \gamma x + \sin \gamma L \cosh \gamma x)$$
$$- \sinh \gamma L (\cos \gamma (L - x) + \sin \gamma L \sinh \gamma x + \cos \gamma L \cosh \gamma x) + \sin \gamma x - \sinh \gamma x)/$$
$$(- \cot \gamma L + (\cot \gamma L - 1) \sinh 2\gamma L + (\cot \gamma L - 1) \cosh 2\gamma L - 1). \tag{3}$$

The elastic properties of the steel background are given by $\rho = 8000$ kg/m^3, $E = 200$ GPa, and $\nu = 0.3$. The geometric parameters of the plate are also given by $h = 5$ m and $L = 20$ m. Evaluating $\omega = 2\pi f$, for example when $f = [10, 90]$ Hz, the plate motion of harmonic vibration can be seen as solid lines in Fig. 1(c). To ensure the validity, we also conduct a finite element simulator COMSOL using a mathematical module. In the language of numerical methods, the strong form of Eqs. (1) and (2) is established as

$$\nabla \cdot \boldsymbol{\Gamma}(u) = \mathbf{U}(u), \tag{4}$$

where

$$\boldsymbol{\Gamma}(u) = \left[\frac{\nabla \cdot M}{2\rho h \omega^2/D} \quad \nabla \cdot u \quad -M \right]^{\mathrm{T}}, \tag{5a}$$

$$\mathbf{U}(u) = [u \quad M \quad Q]^{\mathrm{T}}. \tag{5b}$$

It properly reads in a weak form and can be written as the following:

$$\int_\Omega [\nabla(\Sigma_j \upsilon_j \phi_j(x)) \cdot \boldsymbol{\Gamma}(u) + (\Sigma_j \upsilon_j \phi_j(x)) \mathbf{U}(u)] d\Omega, \tag{6}$$
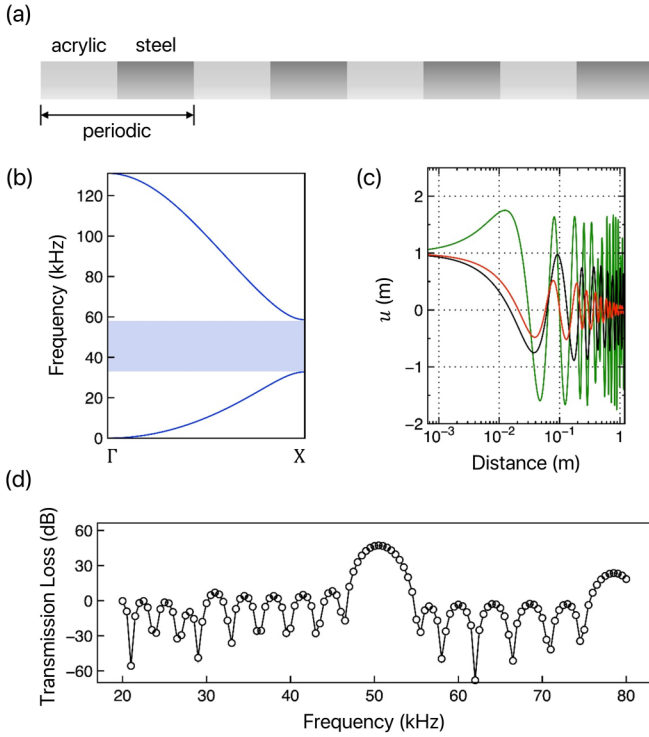
FIG. 2. (a) Schematic of multilayered PCs composed of acrylic and steel in a periodic manner. (b) Band structure calculated by plane-wave expansion method; the shaded region denotes a bandgap in the irreducible Brillouin zone. (c) Out-of-plane displacement fields along the distance at the following frequencies: 30 kHz (black), 50 kHz (red), and 70 kHz (green). The significantly suppressed out-of-plane displacement field is obtained at 50 kHz, as is anticipated in (b). (d) Transmission loss along frequency clearly illustrates the bandgap feature around 50 kHz.

where Ω is the volume element, and $\upsilon(x) = \Sigma_j \upsilon_j \phi_j(x)$ is the test function which is the linear sum of linear Lagrange basis function $\phi_j(x)$ with a node j. The numerical results [Fig. 1(c), dotted square] of the displacement field are well consistent with the analytical solutions. Figure 1(d) indicates the numeric calculation of the stiffness matrix **K** solving $\mathbf{KU} = \mathbf{F}$ where the load vector **F** corresponds to the boundary conditions. The values of **K** become valid that are well-localized along the diagonal elements while computing a larger matrix truncated up to the number of $j \times \mathbf{U}$ with node $j \in \{1, 2, ..., 12\}$ and unknown variables $\mathbf{U} \in \{1, 2, 3\}$. Consideration of the boundary conditions will remain unchanged while further utilizing multilayered PCs. It is worth noting that if a slope boundary (e.g., $\theta = \partial u/\partial x$) is enforced, we need one more variable, which is not mentioned here.

III. BAND CALCULATION

We use multilayered PCs with Bragg gaps endowed by lattice scattering to hinder flexural-type Lamb wave motion. The proposed design is constructed of periodic soft-rigid unit cells, as shown in Fig. 2(a), with $N = 6$ being the total number of periodic unit cells. Within the alternative periodic system, we can evaluate the PCs by the planewave expansion method

using the Fourier expansion of u and Bloch's theorem. We recall the biharmonic equation $\partial^4 u/\partial x^4 = \gamma^4 u$, and separate it and define two parameters α and β for choosing Fourier coefficients

$$\underbrace{\frac{2h^3 E}{3(1 - \nu^2)}}_{\beta} \frac{\partial^4 u}{\partial x^4} = \underbrace{2\rho h}_{\alpha} \omega^2 u. \tag{7}$$

Herein, we apply the spatial harmonic dependence on u as

$$u(\mathbf{x}) = u_{\mathbf{k}} e^{i\mathbf{k}\cdot\mathbf{x}} = \sum_{\mathbf{G}} u(\mathbf{G}) e^{i(\mathbf{k}+\mathbf{G})\cdot\mathbf{x}}, \tag{8}$$

where the Bloch function $u_{\mathbf{k}}$ satisfies the Born–von Karman boundary condition, which is formulated by Fourier series expansion with the reciprocal lattice vector $\mathbf{G}$ $(= \frac{2\pi}{L_{\text{unit cell}}} n_x \hat{\mathbf{x}})$ where n_x is allowed to be integers. Likewise, we can expand the material parameters in Fourier series as $\sigma = \Sigma_{\mathbf{G}}\sigma(\mathbf{G})e^{i\mathbf{G}\cdot\mathbf{x}}$ where σ is a pair of each material parameter [equivalently, $\sigma = (\alpha, \beta)$]. In an effective averaging sense, we have the following relation:

$$\sigma(\mathbf{G}) = \begin{cases} \sigma_A \tilde{f} + \sigma_B(1 - \tilde{f}) & \text{for } \mathbf{G} = 0 \\ (\sigma_A - \sigma_B)F(\mathbf{G}) & \text{for } \mathbf{G} \neq 0, \end{cases} \tag{9}$$

where $\tilde{f} = L_A/L_{\text{uc}}$ is the filling fraction. L_A and $L_{\text{uc}}(= L_A + L_B)$ indicate the length of inclusion and the unit cell, respectively. The subscripts A and B represent each part of the inclusion (or acrylic) and host (or steel). The structure factor $F(\mathbf{G})$ is defined by

$$F(\mathbf{G}) = \frac{1}{L_{\text{uc}}} \int_{L_A} e^{-i\mathbf{G}\cdot\mathbf{x}} dx, \tag{10}$$

where it gives rise to $\tilde{f}\text{sinc}(n\pi\tilde{f})$ by integrating over the length of inclusion. Plugging u and σ in Fourier series into Eq. (7), we obtain

$$\sum_{\mathbf{G}'} [\beta(\mathbf{G} - \mathbf{G}')(\mathbf{k} + \mathbf{G})^2(\mathbf{k} + \mathbf{G}')^2$$
$$- \omega^2\alpha(\mathbf{G} - \mathbf{G}')]u(\mathbf{G}') = 0, \tag{11}$$

where the eigenvalue problem is formulated with $\omega^2(\mathbf{k})$ to be evaluated. For the host part, the steel properties remain the same as in the previous case. We determine the material properties of the inclusion as acrylic; $\rho = 2400$ kg/m^3, $E = 30$ GPa, and $\nu = 0.15$. By letting $L_{\text{unit cell}}$ and L_A hold 20 cm and 10 cm with $h = 5$ cm, the band structure can be achieved for Γ-X in 1D case while searching $\mathbf{k}$ in the irreducible Brillouin zone [Fig. 2(b)]. The suppressed out-of-plane displacement fields are clearly confirmed in the bandgap-induced frequency window [Fig. 2(c), red]; otherwise, the flexural wave remains in the propagating state [Fig. 2(c), black and green]. Transmission loss (TL) is also estimated in Fig. 2(d) by $20\log_{10}(|u_{\text{in}}/u_{\text{out}}|)$, indicating that the positive-valued large peaks arise in the central bandgap frequency range.

IV. ZAK PHASE

Topological engineering is receiving a lot of attention due to the potential pathway to transport wave energy without

losses and backscattering derived from the bulk-boundary correspondence for 2D systems. Handling the geometric phase known as the Zak phase for 1D periodic systems also yields intriguing states with quantized singular states in the bulk band across the Bloch states that are highly localized at interfaces.

Periodic multilayered PCs with no mirror symmetry may provide a representative platform for elastic wave suppression. However, this system is topologically trivial, as there is no interface state within the Bragg gap between the upper and lower bands. Interestingly, by breaking the inversion symmetry (or parity symmetry, $\mathcal{P}$) and incorporating two different geometry phases mirroring each section, we can achieve an interface state that allows for the enhancement of out-of-plane displacement fields [Fig. 3(a)] inside the topological bandgap. The discriminator, the Zak phase which is the analog of the Berry phase for 1D case, is used to classify whether it is topologically invariant or not. The Zak phase in Eq. (12) [52,53]

$$\theta_n^{\text{zak}} = \int_{-\pi/L_{uc}}^{\pi/L_{uc}} \left[i \int_{\text{uc}} \frac{1}{2\rho \text{v}^2} dx u_{n,k}^*(x) \partial_k u_{n,k}(x) \right] dk \quad (12a)$$

$$\approx -\text{Im} \sum_{i=1}^{N} \ln \left[\frac{1}{2\rho \text{v}^2} \int_{uc} dx u_{n,k_i}^*(x) u_{n,k_{i+1}}(x) \right] \quad (12b)$$

takes two quantized values either 0 or π when an intrinsically built-in inversion symmetry broken unit cell is employed. Note that we preserve the same boundary conditions at both ends without loss of generality. The Zak phase is calculated using a discrete formula for numerical computing by integrating over the Berry connection along the single wavevector axis [Eq. (12b)]. In Fig. 3(b), the broken inversion symmetry yields two discrete values, and along the structural variation, the topological phase transition of the second band is observed so that the values change abruptly from π to 0. The elastic weight function $1/(2\rho \text{v}^2)$ does not undergo any change in the Zak phase as long as it is real-valued constant. According to Fig. 3(c), there is a band inversion and the bandgap opens around $\delta=0$, exhibiting a symmetric (antisymmetric) Bloch mode at the upper (lower) band edge for $\delta < 0$. Red and blue square dots represent symmetric and antisymmetric modes, respectively. Each band mode shape at $\delta = \pm 0.02$ is illustrated in the insets, and it can be seen that when $\delta > 0$, the symmetries of displacement fields swap, indicating that it is topologically nontrivial bandgap formation.

To figure out the interface state, we construct mirror symmetry PCs with $N = 6$, where N is the total number of two different unit cells, $\overrightarrow{\text{uc}}$ and $\overleftarrow{\text{uc}}$, based on the origin O. The concise toy model indeed reveals that the localized interface state can be found by the normalized absolute square of displacement field $|u|^2$ emerging geometric phase transition at 52.55 kHz (red solid line), whereas the zoom-in data such as black and green solid lines at 30 and 70 kHz are pointless in the absence of such a phase transition [Fig. 3(d)]. We calculate an averaging intensity $I_{\text{avg}} = \frac{\overleftarrow{\text{uc}}+\overrightarrow{\text{uc}}}{2} \int_{\overleftarrow{\text{uc}}/2}^{\overrightarrow{\text{uc}}/2} |u(x)|^2 dx$ integrating over the interparticle distance that occupies the rigid-rigid section. In Fig. 3(e), extremely large value $I_{\text{avg}} \approx 10^4$ is obtained at the interface state. This also leads to a strong dip in
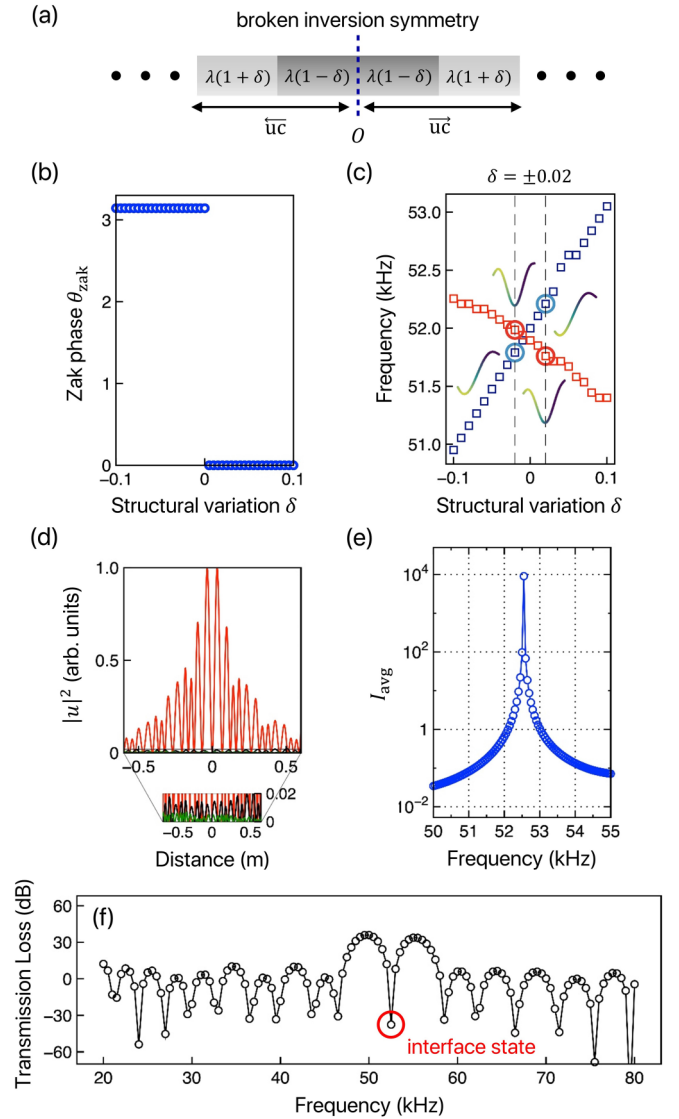

FIG. 3. (a) Schematic of PCs with broken inversion symmetry incorporating different periodic configurations $\overrightarrow{\text{uc}}$ and $\overleftarrow{\text{uc}}$ based on O where $2\lambda = L_{uc}$ and δ is the structural variation, resulting in Zak phase transition that is computed in (b). The abrupt change of Zak phase is achieved near $\delta = 0$, ensuring a topological interface state. (c) Band inversion of the bandgap around 52 kHz with varying the structual variation δ, the red and blue square dots correspond to symmetric and antisymmetric modes, respectively. The insets indicate that the symmetries of displacement fields are inverted. (d) Normalized absolute square of displacement fields for $N = 6$. Highly localized state is observed at the interface at 52.55 kHz (red); otherwise, the fields typically behave governed by boundary conditions. (e) Averaging intensity along frequency reveals the exact value of how it is localized, with an amount of approximately 10^4. (f) Transmission loss along frequencies indicates the feature of the interface state with a strong dip that was previously suppressed owing to the trivial bulk bandgap.

transmission loss [Fig. 3(f), red circle], which was originally suppressed in the trivial bulk band by periodic PCs across the frequency spectra. Note that the presented technique is

not valid for changes involving out-of-plane symmetry along the thickness direction, as we are considering, analytically and numerically, a 1D problem.

V. VOLTAGE FEEDER

Unless we are aware of the exact site of the vibration source, the way in which external stimuli affect the internal system becomes essential in most natural vibration environments. This concern motivates the study on how boundary conditions interact with the main system in topological engineering. Rather than imposing an artificial preload at the interface, we applied boundary constraints on both ends. We therefore can reveal the coupling of the evanescent waves caused by the Bragg gap in the half-frontal system. The evanescent waves are obviously out of reach of the coupling at the interface for $N = 20$ when the number of unit cells N is modulated [Fig. 4(a)]. For $N = 10$, on the other hand, the well-balanced interface state arises, but the intensity at the interface is comparable to that of the fore-end applied by the simply supported boundary condition [Fig. 4(b)]. As a result, measuring the amount to which evanescent waves interact with the interface is critical. Qualitatively, a well-localized state with size compactness, such as $N = 6$, should be sought [Fig. 4(c)]. The trimer-like state with two maxima in the vicinity of the interface is originating from a dimerized scheme of Su-Schrieffer-Heeger chain linked by strong hopping strengths that correspond to rigid-rigid mixture on the continuum side [49,54]. Figure 4(d) indicates that the normalized amplification ratio $u_{\max}/u_{\text{in}}$ estimated by the maximum peak on the amplitude of displacement fields ranged in the rigid-rigid mixture around the interface. The maximum value of 156.71 at 52.55 kHz in the topological plate implies that the vibration is extremely confined. To differentiate the performance of the topological plate from other resonances by global modes, we compare it to the case of the acrylic bare plate (black square dot) for comparison. We find that the amplification ratio of topological plates is much greater than that of acrylic bare plates, as well as at other frequency spans.

The amount of intensity enhancement can be used as an alternative to energy capture to overcome the limits of the mechanical-electric conversion efficiency of piezoelectric materials [Fig. 4(e)]. For practical purposes, an inset schematic is presented, which comprises of a piezoelectric material (PZT-4) with ground and terminal electrodes mounted on topological mirror-symmetric PCs at the interface. The voltage can be retrieved by the relation $V = dFt/(\varepsilon_r \varepsilon_0 A)$ where $d(= 2.95 \times 10^{-10}\,\text{m/V})$ is the piezoelectric coefficient, $F = \sigma A(= 1\,\text{N})$ is the force, $t(= 5\,\text{mm})$ is the thickness, $\varepsilon_r(= 1300)$ is relative permittivity, $\varepsilon_0(= 8.85 \times 10^{-12}\,\text{F}\,\text{m}^{-1})$ is the vacuum permittivity, and $A(= 1\,\text{cm} \times 10\,\text{cm})$ is the area. Note that we determined $u|_{x=0} \approx 1.07132 \times 10^{-9}\,\text{m}$ at the simply supported boundary condition that corresponds to $F \approx 1\,\text{N}$ extracted through the relations $\mathbf{e} = \frac{1}{2}(\nabla\mathbf{u} + (\nabla\mathbf{u})^{\text{T}})$ and $\boldsymbol{\sigma} = \lambda\text{Tr}(\mathbf{e})\mathbf{I} + 2\mu\mathbf{e}$ where $\mathbf{e}$ is the strain and $\boldsymbol{\sigma}$ is the stress, and λ and μ are the Lamé parameters. It reveals that the large voltage, approximately 20 V, induced by the interface state can be obtained from the compact size of the piezoelectric material [Fig. 4(f)]. The voltage feeder
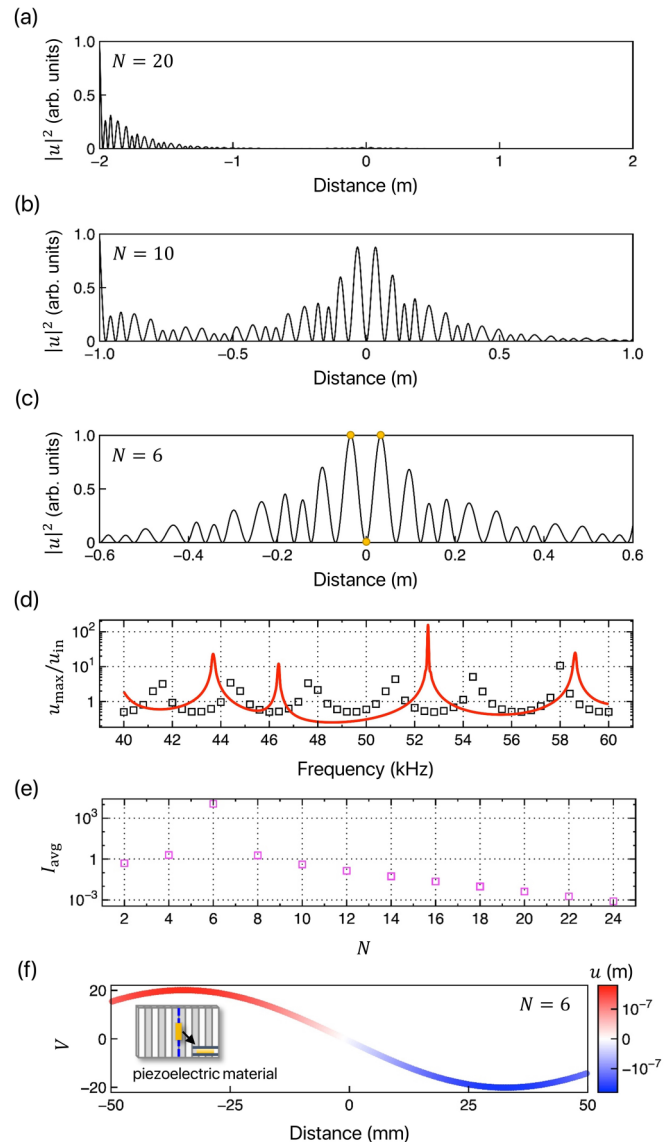

FIG. 4. Normalized absolute square of displacement fields for (a) $N = 20$, (b) $N = 10$, and (c) $N = 6$, respectively. (a) The large number of N causes evanescent waves that are unable to reach the interface due to the bandgap, while (b) the case of $N = 10$ indicates the well-balanced interface state emerges as a result of the coupling of evanescent waves, although the intensity is almost in unity arising from the left boundary condition. (c) Optimized case with a trimer-like state (yellow circles) and two maxima for $N = 6$, resulting in the strong confinement at the interface. (d) Amplification ratio $u_{\max}/u_{\text{in}}$ (red solid line) for the optimal case of $N = 6$. The black square dots represent the acrylic bare plate for comparison. At 52.55 kHz, the maximum amplification ratio is reached in topological plates. (e) Averaging intensity along N shows that an optimal configuration, such as $N = 6$, should be sought. (f) Voltage at the site surrounding O where the piezoelectric material sandwiched by two electrodes is placed. The voltage levels around 20 V induced by the topological interface state are indeed substantial, and may possibly be exploited for energy harvesting.

established by the topological engineering strategy, which expands the scale from millivolts to volts, may outperform recently developed methods such as gradient index lenses,

local resonators, and defect-based PCs based on subwavelength microstructures.

VI. CONCLUDING REMARKS

The rapid improvement in designing topological edge/interface states has captivated the desire of topological photonic and phononic systems inspired from the electronic equivalents. However, electromagnetic/acoustic waves in topological engineering are described by 2D PDEs, which cannot be easily applied to thin plate motions in classic wave models. Therefore, we provide a 1D elastic topological interface state generated by breaking the inversion symmetry for flexural waves on thin plate frameworks, filling a knowledge gap in 4D PDEs. We propose an interface state based on elastic phononic crystals (PCs) by harnessing mirror symmetry. The plane-wave expansion method is used to construct topologically trivial multilayered PCs, which result in typical bandgap features. When the inversion symmetry of a system is broken, a geometric phase transition (also known as the Zak phase) takes place, resulting in a localized interface state. With respect to energy harvesting, we investigate at whether or not the localized state can be leveraged as a voltage feeder. According to our findings, an optimal system should account for evanescent wave couplings between the input and interface in order to obtain high voltages and highly confined waves.

[1] H. Liu, J. Zhong, C. Lee, S.-W. Lee, and L. Lin, Appl. Phys. Rev. **5**, 041306 (2018).

[2] S. Priya, Appl. Phys. Lett. **87**, 184101 (2005).

[3] A. Erturk and D. J. Inman, J. Vib. Acoust. Trans. ASME **130**, 041002 (2008).

[4] A. Erturk and D. J. Inman, Smart Mater. Struct. **18**, 025009 (2009).

[5] A. Erturk, J. Hoffmann, and D. J. Inman, Appl. Phys. Lett. **94**, 254102 (2009).

[6] X. Gao, W.-H. Shih, and W. Y. Shih, Appl. Phys. Lett. **97**, 233503 (2010).

[7] S.-C. S. Lin, T. J. Huang, J.-H. Sun, and T.-T. Wu, Phys. Rev. B **79**, 094302 (2009).

[8] T.-T. Wu, Y.-T. Chen, J.-H. Sun, S.-C. S. Lin, and T. J. Huang, Appl. Phys. Lett. **98**, 171911 (2011).

[9] J. Zhao, R. Marchal, B. Bonello, and O. Boyko, Appl. Phys. Lett. **101**, 261905 (2012).

[10] S. Tol, F. L. Degertekin, and A. Erturk, Appl. Phys. Lett. **109**, 063902 (2016).

[11] S. Tol, F. Degertekin, and A. Erturk, Appl. Phys. Lett. **111**, 013503 (2017).

[12] J. Hyun, W. Choi, and M. Kim, Appl. Phys. Lett. **115**, 173901 (2019).

[13] A. Allam, K. Sabra, and A. Erturk, Appl. Phys. Lett. **118**, 103504 (2021).

[14] S. Gonella, A. C. To, and W. K. Liu, J. Mech. Phys. Solids **57**, 621 (2009).

[15] K. Mikoshiba, J. M. Manimala, and C. Sun, J. Intell. Mater. Syst. Struct. **24**, 168 (2013).

[16] G. Hu, L. Tang, and R. Das, J. Appl. Phys. **123**, 055107 (2018).

[17] G. Hu, L. Tang, J. Xu, C. Lan, and R. Das, J. Appl. Mech. **86**, 081009 (2019).

[18] M. Alshaqaq and A. Erturk, Smart Mater. Struct. **30**, 015029 (2021).

[19] L.-Y. Wu, L.-W. Chen, and C.-M. Liu, Appl. Phys. Lett. **95**, 013506 (2009).

[20] H. Lv, X. Tian, M. Y. Wang, and D. Li, Appl. Phys. Lett. **102**, 034103 (2013).

[21] S. Qi, M. Oudich, Y. Li, and B. Assouar, Appl. Phys. Lett. **108**, 263501 (2016).

[22] S.-H. Jo, H. Yoon, Y. C. Shin, W. Choi, C.-S. Park, M. Kim, and B. D. Youn, Int. J. Mech. Sci. **179**, 105670 (2020).

[23] T.-X. Ma, Q.-S. Fan, Z.-Y. Li, C. Zhang, and Y.-S. Wang, Extreme Mech. Lett. **41**, 101073 (2020).

[24] S.-H. Jo, H. Yoon, Y. C. Shin, M. Kim, and B. D. Youn, J. Appl. Phys. **127**, 164901 (2020).

[25] T.-G. Lee, S.-H. Jo, H. M. Seung, S.-W. Kim, E.-J. Kim, B. D. Youn, S. Nahm, and M. Kim, Nano Energy **78**, 105226 (2020).

[26] G. Lee, D. Lee, J. Park, Y. Jang, M. Kim, and J. Rho, Commun. Phys. **5**, 1 (2022).

[27] L. Cao, Y. Zhu, Y. Xu, S.-W. Fan, Z. Yang, and B. Assouar, J. Mech. Phys. Solids **154**, 104502 (2021).

[28] L. Cao, Y. Zhu, S. Wan, Y. Zeng, Y. Li, and B. Assouar, Extreme Mech. Lett. **47**, 101364 (2021).

[29] M. Xiao, Z. Q. Zhang, and C. T. Chan, Phys. Rev. X **4**, 021017 (2014).

[30] P. Wang, L. Lu, and K. Bertoldi, Phys. Rev. Lett. **115**, 104302 (2015).

[31] L. M. Nash, D. Kleckner, A. Read, V. Vitelli, A. M. Turner, and W. T. Irvine, Proc. Natl. Acad. Sci. USA **112**, 14495 (2015).

[32] S. H. Mousavi, A. B. Khanikaev, and Z. Wang, Nat. Commun. **6**, 8682 (2015).

[33] S. Li, D. Zhao, H. Niu, X. Zhu, and J. Zang, Nat. Commun. **9**, 1370 (2018).

[34] R. K. Pal and M. Ruzzene, New J. Phys. **19**, 025001 (2017).

[35] D. Zhao, M. Xiao, C. W. Ling, C. T. Chan, and K. H. Fung, Phys. Rev. B **98**, 014110 (2018).

[36] S.-Y. Yu, C. He, Z. Wang, F.-K. Liu, X.-C. Sun, Z. Li, H.-Z. Lu, M.-H. Lu, X.-P. Liu, and Y.-F. Chen, Nat. Commun. **9**, 3072 (2018).

[37] M. Miniaci, R. K. Pal, B. Morvan, and M. Ruzzene, Phys. Rev. X **8**, 031074 (2018).

[38] X. Wu, Y. Meng, Y. Hao, R.-Y. Zhang, J. Li, and X. Zhang, Phys. Rev. Lett. **126**, 226802 (2021).

[39] K. v. Klitzing, G. Dorda, and M. Pepper, Phys. Rev. Lett. **45**, 494 (1980).

[40] R. B. Laughlin, Phys. Rev. B **23**, 5632 (1981).

[41] D. J. Thouless, M. Kohmoto, M. P. Nightingale, and M. den Nijs, Phys. Rev. Lett. **49**, 405 (1982).

[42] M. Esmann, F. R. Lamberti, A. Lemaître, and N. D. Lanzillotti-Kimura, Phys. Rev. B **98**, 161109(R) (2018).

[43] M. Esmann, F. R. Lamberti, P. Senellart, I. Favero, O. Krebs, L. Lanco, C. Gomez Carbonell, A. Lemaître, and N. D. Lanzillotti-Kimura, Phys. Rev. B **97**, 155422 (2018).

[44] O. Ortiz, P. Priya, A. Rodriguez, A. Lemaitre, M. Esmann, and N. Lanzillotti-Kimura, Optica **8**, 598 (2021).

[45] J. Vila, R. K. Pal, and M. Ruzzene, Phys. Rev. B **96**, 134307 (2017).

[46] M. Miniaci, R. K. Pal, R. Manna, and M. Ruzzene, Phys. Rev. B **100**, 024304 (2019).

[47] G. Ma, M. Xiao, and C. T. Chan, Nat. Rev. Phys. **1**, 281 (2019).

[48] M. Miniaci and R. K. Pal, J. Appl. Phys. **130**, 141101 (2021).

[49] M. Esmann and N. D. Lanzillotti-Kimura, Appl. Sci. **8**, 527 (2018).

[50] X. Shi, I. Kiorpelidis, R. Chaunsali, V. Achilleos, G. Theocharis, and J. Yang, Phys. Rev. Res. **3**, 033012 (2021).

[51] A. Cabada, J. A. Cid, and L. Sanchez, Nonlinear Analysis: Theory, Methods & Applications **67**, 1599 (2007).

[52] J. Zak, Phys. Rev. Lett. **62**, 2747 (1989).

[53] M. Xiao, G. Ma, Z. Yang, P. Sheng, Z. Zhang, and C. T. Chan, Nat. Phys. **11**, 240 (2015).

[54] R. Chaunsali, E. Kim, A. Thakkar, P. G. Kevrekidis, and J. Yang, Phys. Rev. Lett. **119**, 024301 (2017).